

# Array FBG sensing and 3D reconstruction of spacecraft configuration\*

JIANG Yue<sup>1</sup>, YAN Jie<sup>1</sup>, ZHANG Lei<sup>1\*\*</sup>, JIANG Mingshun<sup>1</sup>, LUO Yuxiang<sup>2</sup>, and SUI Qingmei<sup>1</sup>

1. School of Control Science and Engineering, Shandong University, Jinan 250061, China

2. Shandong Institute of Space Electronic Technology, Yantai 264003, China

(Received 4 June 2021; Revised 27 November 2021)

©Tianjin University of Technology 2022

In this paper, a plate shape perception technique based on quasi-distributed fiber Bragg grating (FBG) array and space surface reconstruction algorithm is proposed. Firstly, in order to make curvature continuous, the bicubic plane interpolation algorithm is studied. Then, taking the simulated satellite bulkhead structure as the research object, we research the space surface reconstruction algorithm based on orthogonal curvature and coordinate transformation (translation and rotation). Finally, a four-sided fixed plate deformation monitoring system based on quasi-distributed FBG sensors network and surface reconstruction algorithm is built. Many experiments are conducted to verify the reliability and accuracy of the algorithm. The proposed algorithm provides a new method for three-dimensional reconstruction of spacecraft structure.

**Document code:** A **Article ID:** 1673-1905(2022)04-0193-7

**DOI** <https://doi.org/10.1007/s11801-022-1090-1>

During the operation of spacecraft, due to the interference of internal excitation and external environment, structural shape deformation occurs easily. Especially in the case of long-term high intensity flight, the large deformation over a long time will cause structural fatigue damage, reduce its stability, and even lead to failure<sup>[1,2]</sup>. Therefore, it is of great significance to monitor the spacecraft structural shape during operation and make corresponding adjustment strategies in time<sup>[3,4]</sup>. At present, spacecrafts mostly use large area, high strength and light flexible materials<sup>[5]</sup>, and the complex working environment requires that sensing devices have good compatibility. The traditional deformation monitoring methods include photogrammetry, strain measurement, acceleration sensors measurement<sup>[6]</sup>. However, due to large volume, poor anti-electromagnetic interference ability, and inability to real-time requirements, they were gradually replaced by optical fiber sensors measurement.

NISHIO et al<sup>[7]</sup> reconstructed the deformation morphology of composite laminated plates by using fiber optic sensors. NISHIYAMA et al<sup>[8]</sup> used hetero-core fiber optic sensors to monitor the large deformation of the smart plate structure and read the bending direction. KANG et al<sup>[9]</sup> studied the deformation morphology monitoring method of flexible rod structures by using fiber Bragg grating (FBG) wavelength-division multiplexing (WDM) technology. QIAO et al<sup>[10]</sup> realized the reconstruction of flexible plate structure by surface

patches splicing.

Most of the above researches directly use orthogonal distributed sensors to monitor the deformation morphology of rod structure and plate structure, while few researches use non-orthogonal distributed sensors to invert four-sided fixed plate structure. In this paper, taking the simulated satellite bulkhead structure as the research object, the quasi-distributed sensing network is constructed by using FBG sensors and WDM network layout. Then the central wavelength offsets of sensors are converted into the orthogonal curvature information by the bicubic plane interpolation algorithm. The structural shape based on the spatial coordinate transformation algorithm can be reconstructed to achieve the goal of high-precision monitoring of the deformation morphology of the bulkhead structure.

When a beam of incident light is transmitted in the fiber grating, mode coupling occurs, reflecting the light that corresponds to the Bragg condition<sup>[11]</sup>. The grating central wavelength  $\lambda_B$  can be obtained by effective refractive index  $n_{\text{eff}}$  and grating period  $\Lambda$  as

$$\lambda_B = 2n_{\text{eff}}\Lambda. \quad (1)$$

Ignoring the temperature change, the FBG center wavelength change caused by axial strain is

$$\Delta\lambda_B/\lambda_B = (1 - P_e)\epsilon, \quad (2)$$

where  $P_e$  denotes the elasto-optical coefficient (0.22 for

\* This work has been supported by the National Natural Science Foundation of China (Nos.62073193 and 61873333), the Key Research and Development Plan of Shandong Province (Nos.2019TSLH0301 and 2019GHZ004), and the Natural Science Foundation of Shandong Province (No.ZR2021MF041).

\*\* E-mail: drleizhang@sdu.edu.cn

silica). It shows that there is a certain linear relationship between strain and FBG wavelength offset<sup>[12,13]</sup>.

The thickness of the structure is far less than its length and width, so it can be considered as a thin plate. We paste the FBG sensors on the structure surface. When the sensor is subjected to external force, we can obtain the structural strain.

Along the axial direction of the FBG sensor, take the micro element segment with the length  $L$  and width  $h$ . When the micro element segment is subjected to external mechanical force, the upper end face is stretched into  $(L + \Delta L)$  by tension, as shown in Fig.1.

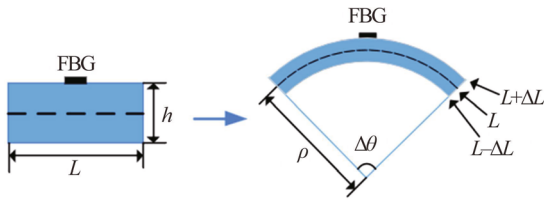


**Fig.1 Curvature relationship of the FBG**

In Fig.1, the original length  $L$  and the upper end face length  $(L + \Delta L)$  can be calculated as

$$\begin{cases} L = \rho \Delta \theta \\ L + \Delta L = (\rho + \frac{h}{2}) \Delta \theta \end{cases} \quad (3)$$

where  $\rho$  is the curvature radius, and  $\Delta \theta$  is the corresponding arc angle. According to the strain formula  $\varepsilon = \Delta L / L$ , the curvature  $k$  can be expressed as

$$k = \frac{1}{\rho} = \frac{2}{h} \times \frac{\Delta L}{L} = \frac{2}{h} \varepsilon, \quad (4)$$

which clearly shows that the curvature changes linearly with the strain.

According to Eqs.(2) and (4), keeping the thickness of structure constant, the curvature is linearly related to the FBG wavelength offset.

The small number of FBG sensors on the bulkhead structure makes it difficult to obtain smooth deformation surface. Therefore, appropriate interpolation algorithm is needed to deal with the discrete curvature. LI et al<sup>[14]</sup> adopted linear interpolation to get the tubular structural deformation curves. WANG et al<sup>[15]</sup> obtained the continuous curvature of the soft manipulator by using B-spline interpolation.

The bulkhead surface is smooth and non-abrupt under pressure, so the discrete curvature can be transformed into continuous curvature by plane interpolation method. In this paper, the bicubic interpolation method is used to process discrete curvature.

In the bicubic interpolation method, select 12 points closest to the interpolation point as the reference points, as shown in Fig.2.

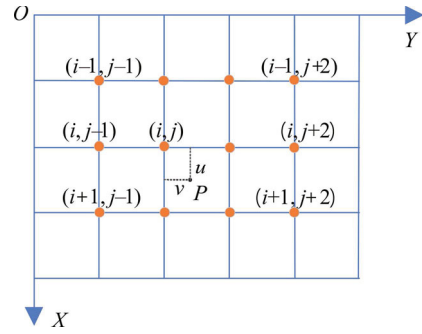


**Fig.2 Schematic diagram of bicubic interpolation**

In Fig.2,  $P$  is the point to be interpolated, and its coordinate may have decimal parts. Assume the coordinate is  $P(i+u, j+v)$ , where  $(i, j)$  is the integer part and  $(u, v)$  is the decimal part. The reference point value is denoted by  $f(i, j)$ ,  $(i, j=0, 1, 2, 3\dots)$ . The value of point  $P$  can be expressed as

$$f(i+u, j+v) = \sum_{a=-1}^1 \sum_{b=-1}^2 f(i+a, j+b) S(|a-u|) S(|b-v|), \quad (5)$$

which is written in matrix form as

$$f(i+u, j+v) = \mathbf{ABC}, \quad (6)$$

where  $\mathbf{A}$ ,  $\mathbf{B}$  and  $\mathbf{C}$  are all matrices, and their forms are respectively as follows

$$\begin{cases} \mathbf{A} = [S(1+u), S(u), S(1-u)] \\ \mathbf{B} = \begin{bmatrix} f(i-1, j-1) & f(i-1, j) & f(i-1, j+1) & f(i-1, j+2) \\ f(i, j-1) & f(i, j) & f(i, j+1) & f(i, j+2) \\ f(i+1, j-1) & f(i+1, j) & f(i+1, j+1) & f(i+1, j+2) \end{bmatrix} \\ \mathbf{C} = [S(1+v), S(v), S(1-v), S(2-v)]^T \end{cases} \quad (7)$$

where  $S(w)$  is the impact factor equation. The formula is as follows

$$S(w) = \begin{cases} \frac{17|w|^3}{9} - \frac{53w^2}{18} + \frac{17|w|}{225} + 1 & 0 \leq |w| < 1 \\ -\frac{|w|^3}{210} + \frac{67w^2}{2100} - \frac{173|w|}{2100} + \frac{79}{1050} & 1 \leq |w| \leq 2 \end{cases} \quad (8)$$

Assume that the bulkhead four-sided fixed plate structural directions are vertical ( $Y$  direction) and horizontal along the board ( $X$  direction). By the bicubic interpolation method, we obtain continuous and orthogonal curvatures (vertical curvature  $k(m)$  and horizontal curvature  $k(n)$ ).  $m$  and  $n$  are the nodes numbers, and all nodes make up an orthogonal network. Using the principle of coordinate transformation, the spatial coordinates of each node can be obtained, and then a smooth deformation surface is reconstructed by surface fitting algorithm.

There are orthogonal curves at nodes, so it is necessary to establish moving coordinate system in both directions simultaneously. The continuity of the curve enables the node coordinates to be obtained by the coordinate system

transformation. The coordinate transformation in  $X$  direction is shown in Fig.3. After point  $P(m, n)$  rotates  $\theta(n, m)$  around the  $Y$  axis and rotates  $\beta(n, m)$  around the  $X$  axis, then it shifts to point  $P(n+1, m)$ . In Fig.3,  $\Delta s$  is the arc length of adjacent nodes, and  $\theta(n, m)$  can be expressed as  $\theta(n, m) = \Delta s / \rho(n, m) = \Delta s \cdot k(n, m)$ .

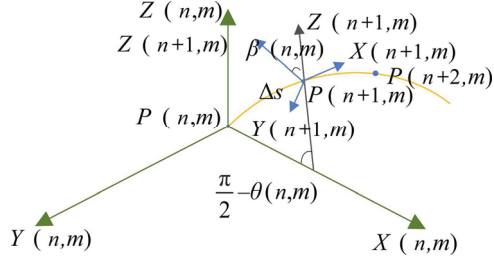


**Fig.3 Diagram of the moving coordinate system transformation**

Set  $P(n, m)$  as the absolute coordinate, and  $P'(n, m)$  as the relative coordinate<sup>[16]</sup>. According to the geometric relationship shown in Fig.3, the relative coordinate of point  $P(n+1, m)$  is

$$\begin{cases} P'_x(n+1, m) = \rho(n, m) \cdot (1 - \sin(\theta(n, m))) \\ P'_y(n+1, m) = 0 \\ P'_z(n+1, m) = \rho(n, m) \cdot \cos(\beta(n, m)) \end{cases}, \quad (9)$$

where set point  $P(1, m)$  as the first node of the curve, and the absolute coordinate system is established from this point. The absolute coordinate of point  $P(2, m)$  equals to relative coordinate and can be expressed as

$$\begin{cases} P_x(2, m) = (1 - \sin(\Delta s \cdot k(1, m))) / k(1, m) \\ P_y(2, m) = 0 \\ P_z(2, m) = \cos(\Delta s \cdot k(1, m)) / k(1, m) \end{cases}. \quad (10)$$

Point  $P(2, m)$  rotates  $\theta(1, m)$  around the  $Y$  axis firstly, and then rotates  $\beta(1, m)$  around the  $X$  axis, getting the relative coordinate system of point  $P(3, m)$ . From this recursion, the absolute coordinate of the point  $P(n, m)$  ( $n > 2$ ) can be calculated as

$$P(n, m) = \left\{ \prod_{i=1}^{n-2} \mathbf{Q}_x(\beta(i, m)) \cdot \mathbf{Q}_y(\theta(i, m)) \right\} \times P'(n, m) + P(n-1, m), \quad (11)$$

where the rotation matrices are respectively

$$\mathbf{Q}_x(\beta) = \begin{bmatrix} \cos \beta & 0 & -\sin \beta \\ 0 & 1 & 0 \\ \sin \beta & 0 & \cos \beta \end{bmatrix}, \quad \mathbf{Q}_y(\theta) = \begin{bmatrix} 1 & 0 & 0 \\ 0 & \cos \theta & \sin \theta \\ 0 & -\sin \theta & \cos \theta \end{bmatrix}. \quad (12)$$

Assume that point  $P(n+1, m+1)$  is the same node in

both coordinate systems, and it is represented by the midpoint in both directions, as shown in Fig.4.  $\beta(n, m)$  can be expressed as

$$\begin{cases} \beta_x(n, m) = \arccg \frac{[\mathbf{R}(x'_x(n, m), y'_x(n, m), z'_x(n, m)) \cdot x'_y(n, m)]_z}{[\mathbf{R}(x'_x(n, m), y'_x(n, m), z'_x(n, m)) \cdot x'_y(n, m)]_x} \\ \beta_y(n, m) = \arccg \frac{[\mathbf{R}(x'_y(n, m), y'_y(n, m), z'_y(n, m)) \cdot x'_x(n, m)]_z}{[\mathbf{R}(x'_y(n, m), y'_y(n, m), z'_y(n, m)) \cdot x'_x(n, m)]_y} \end{cases}, \quad (13)$$

where  $\mathbf{R}(x'_x(n, m), y'_x(n, m), z'_x(n, m))$  represents coordinate vector in the coordinate system  $x'_x(n, m) - y'_x(n, m) - z'_x(n, m)$ .

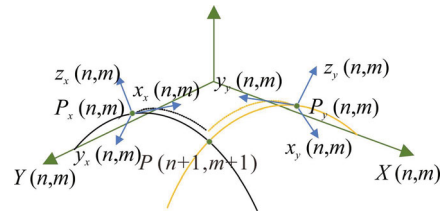


**Fig.4 Diagram of the spatial torsion angle**

In order to complete the coordinate transformation and make the coordinate axis coincide, after the nodes rotate around the  $Y$  axis and the  $X$  axis, they need to rotate  $\gamma$  around the  $Z$  axis. The angle and matrices are

$$\gamma_x(n, m) = \arccg[\mathbf{R}(x'_x(n, m), y'_x(n, m), z'_x(n, m)) \cdot x'_y(n, m)]_x / 2,$$

$$\mathbf{Q}_z(\gamma) = \begin{bmatrix} \cos \gamma & \sin \gamma & 0 \\ -\sin \gamma & \cos \gamma & 0 \\ 0 & 0 & 1 \end{bmatrix}. \quad (14)$$

Therefore, we first get orthogonal curvatures through bicubic interpolation, and then obtain absolute coordinates by coordinate transformation and recursion. Finally, by fitting the absolute coordinates, we form the smooth and continuous deformation surface.

The simulated satellite bulkhead structure deformation reconstruction system consists of bulkhead plates, solar panels, distributed sensors array, fiber grating demodulator, dial indicators and control computer. The experimental system model is shown in Fig.5(a). The bulkhead is a 660 mm × 660 mm × 3 mm aluminum alloy plate. The axial sensors are distributed in 8 rows and 10 columns, and transverse sensors are distributed in 9 rows and 6 columns. The dial indicators with accuracy of 0.002 mm are mounted on the structure surface to obtain the real deformation values of the checking points. The resolution of FBG demodulator is 1 pm, and the scanning frequency is 100 Hz, so it can obtain the wavelength values of the sensors in real time. There are two loading positions, respectively located in the center of the structure and the upper right 2/3 of the structure. The loading tools are the stepping motors 1 and 2. The load area is 60 mm × 60 mm.

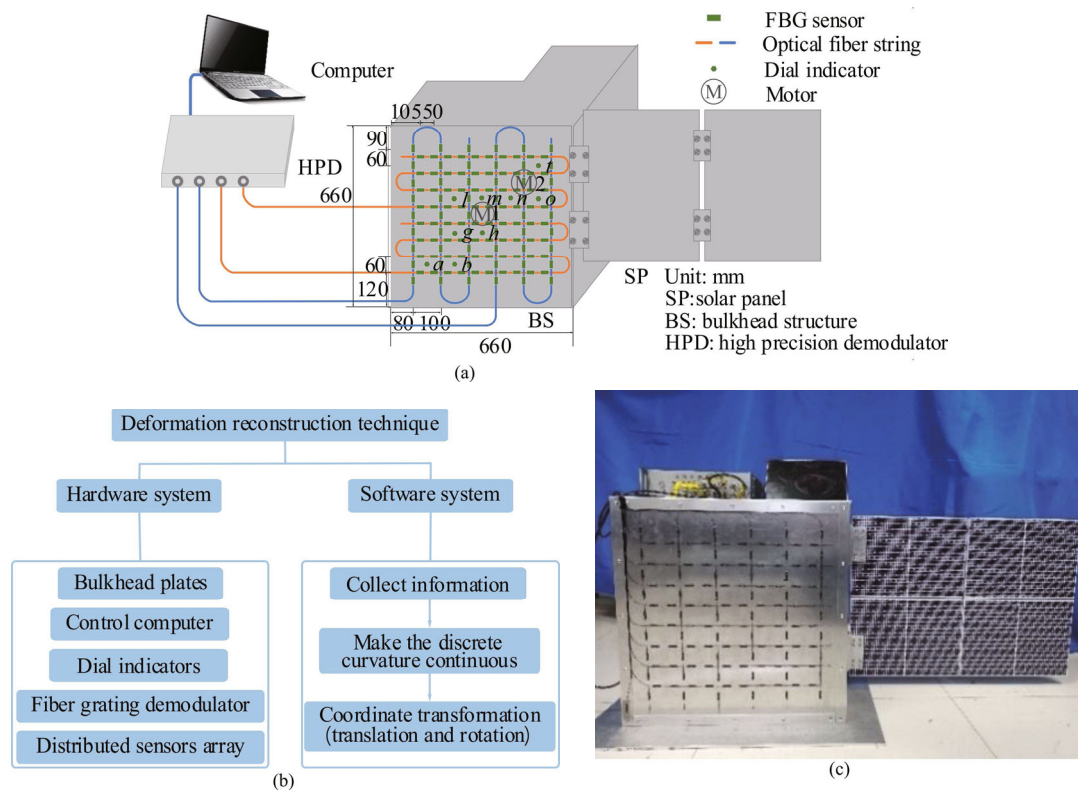


Fig.5 (a) Experimental system model; (b) Flow chart of the system; (c) Experimental system diagram

The stepper motor compresses spring, and the bulk-head structure will deform. We carried out experiments under four loading conditions, as shown in Tab.1.

In this paper, linear interpolation and bicubic interpolation were adopted to reconstruct the structural deformation shape. To verify the reliability of the algorithm, we introduced absolute error, relative error and root-mean-square error to compare the dial indicators values and the reconstructed values at the checking points. We conducted many experiments under each loading condition. The experimental data analysis results are shown in Tab.2.

Tab.1 Loading conditions of the structure

Number	Loading condition	Checking points
1	Only motor 1 applies force gradually	<i>a, b, l, m, n</i>
2	Only motor 2 applies force gradually	<i>a, g, m, n, o</i>
3	Motor 1 reaches maximum force value, while motor 2 gradually applies force	<i>h, m, n, o, t</i>
4	Motor 2 reaches maximum force value, while motor 1 gradually applies force	<i>h, l, m, n, t</i>

Tab.2 Data analysis results of bulkhead structure under different loading conditions

(a) Structural deformation error analysis under the first loading condition

Checking point	Interpolation method	Measured value $D_r$ (mm)	Reconstructed value $D_m$ (mm)	Absolute error $\Delta$ (mm)	Relative error $\sigma$ (%)
<i>a</i>	Linear	0.556	0.588 8	0.032 8	5.899
	Double cubic		0.549 3	0.006 7	1.205
<i>b</i>	Linear	1.267	1.201 0	0.066 0	5.209
	Double cubic		1.253 9	0.013 1	1.034
<i>l</i>	Linear	2.483	2.669 0	0.186 0	7.491
	Double cubic		2.450 6	0.032 4	1.305
<i>m</i>	Linear	3.280	3.080 5	0.199 5	6.082
	Double cubic		3.237 1	0.042 9	1.308
<i>n</i>	Linear	2.548	2.377 0	0.171 0	6.711
	Double cubic		2.576 6	0.028 6	1.122

(b) Structural deformation error analysis under the second loading condition

Checking point	Interpolation method	Measured value	Reconstructed value	Absolute error	Relative error
		$D_r$ (mm)	$D_m$ (mm)	$\Delta$ (mm)	$\sigma$ (%)
<i>a</i>	Linear	0.025	0.023 7	0.001 3	5.200
	Double cubic		0.025 3	0.000 3	1.200
<i>g</i>	Linear	0.471	0.455 3	0.015 7	3.333
	Double cubic		0.479 1	0.008 1	1.720
<i>m</i>	Linear	1.274	1.317 8	0.043 8	3.438
	Double cubic		1.251 6	0.022 4	1.758
<i>n</i>	Linear	1.957	2.019 8	0.062 8	3.209
	Double cubic		1.991 5	0.034 5	1.763
<i>o</i>	Linear	1.524	1.473 7	0.050 3	3.301
	Double cubic		1.555 2	0.031 2	2.047

(c) Structural deformation error analysis under the third loading condition

Checking point	Interpolation method	Measured value	Reconstructed value	Absolute error	Relative error
		$D_r$ (mm)	$D_m$ (mm)	$\Delta$ (mm)	$\sigma$ (%)
<i>h</i>	Linear	3.465	3.603 0	0.138 0	3.983
	Double cubic		3.417 0	0.048 0	1.385
<i>m</i>	Linear	3.981	3.736 0	0.245 0	6.154
	Double cubic		4.022 0	0.041 0	1.029
<i>n</i>	Linear	3.510	3.283 0	0.227 0	6.467
	Double cubic		3.474 8	0.035 2	1.003
<i>o</i>	Linear	2.153	2.038 0	0.115 0	5.341
	Double cubic		2.202 0	0.049 0	2.276
<i>t</i>	Linear	1.332	1.412 3	0.080 3	6.029
	Double cubic		1.308 0	0.024 0	1.802

(d) Structural deformation error analysis under the fourth loading condition

Checking point	Interpolation method	Measured value	Reconstructed value	Absolute error	Relative error
		$D_r$ (mm)	$D_m$ (mm)	$\Delta$ (mm)	$\sigma$ (%)
<i>h</i>	Linear	3.383	3.241 4	0.141 6	4.186
	Double cubic		3.366 0	0.017 0	0.503
<i>l</i>	Linear	2.489	2.363 9	0.125 1	5.026
	Double cubic		2.456 5	0.032 5	1.306
<i>m</i>	Linear	3.532	3.318 5	0.213 5	6.045
	Double cubic		3.578 3	0.046 3	1.311
<i>n</i>	Linear	3.173	3.001 0	0.172 0	5.421
	Double cubic		3.210 0	0.037 0	1.166
<i>t</i>	Linear	1.069	0.987 0	0.082 0	7.671
	Double cubic		1.080 0	0.011 0	1.029

(e) Average error analysis under different loading conditions

Loading condition	Interpolation method	First	Second	Third	Fourth
	Average relative error $\bar{\sigma}$ (%)	Linear	6.278	3.710	5.595
	Double cubic	1.194	1.690	1.499	1.684
Root-mean-square error $\delta$ (mm)	Linear	0.147	0.042	0.173	0.153
	Double cubic	0.028	0.023	0.040	0.032

Under the four loading conditions, with the increasing of the load on the structure, the structural deformation becomes more and more serious. The layout of sensors, interpolation method and temperature affect the reconstruction effect of the deformation algorithm. Keeping the external environment stable, under different loading conditions, the average relative error based on linear interpolation reached 6%, while that based on bicubic interpolation is less than or equal to 1.7%, the overall relative error is less than or equal to 2.3%, the maximum absolute error is 0.049 mm, and the root-mean-square error is less than or equal to 0.04 mm. Obviously, the latter has smaller error, higher accuracy and better effect than the former. Therefore, the reconstruction algorithm based on the bicubic interpolation can better express the deformation shape of the plate structure.

Fig.6 represents the structural reconstruction diagrams based on the bicubic interpolation under four loading conditions. It can be seen that under different loading conditions, the proposed reconstruction algorithm can accurately reflect the structural real deformation shape.

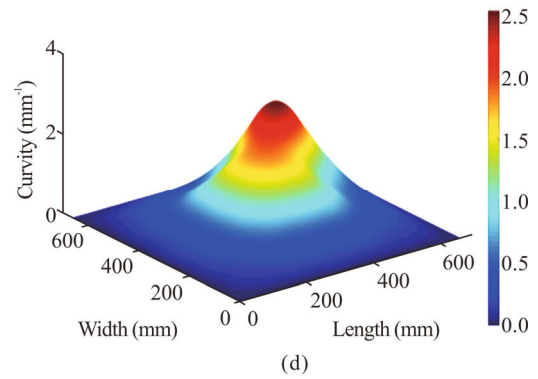
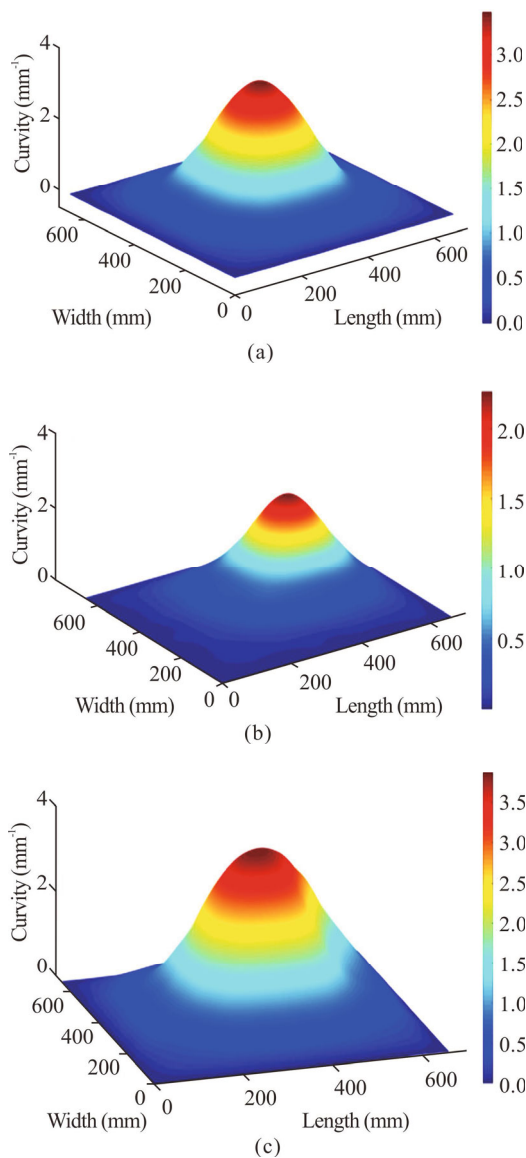


**Fig.6 Deformation surface diagrams with (a) the first loading condition, (b) the second loading condition, (c) the third loading condition, and (d) the fourth loading condition**

In this paper, a high precision deformation monitoring system of the simulated bulkhead structure was built. We used bicubic plane interpolation method and adopted coordinate transformation method to obtain smooth structural deformation surface. After setting up the experimental system, we carried out many experiments under various loading conditions to verify the accuracy of the surface deformation algorithm. Through error analysis, the results show that compared with the linear interpolation method, this algorithm can more accurately realize the spatial deformation monitoring of the plate structure, and has a good prospect of engineering applications.

**Statements and Declarations**

The authors declare that there are no conflicts of interest related to this article.

**References**

- [1] QIU L, FANG F, YUAN S F. Improved density peak clustering-based adaptive Gaussian mixture model for damage monitoring in aircraft structures under time-varying conditions[J]. Mechanical systems and signal processing, 2019, 126: 281-304.
- [2] BEDNARSKA K, SOBOTKA P, WOLINSKI T R, et al. Hybrid fiber optic sensor systems in structural health monitoring in aircraft structures[J]. Materials, 2020, 13(10): 2249-2265.
- [3] MARTINS T, INFANTE V, SOUSA L, et al. Numerical and experimental study of aircraft structural health[J]. International journal of fatigue, 2020, 132: 105348.
- [4] LIU X M, GE Y T, YIN X T. On health monitor technology development for damaged aircraft structures[J]. Applied mechanics and materials, 2013, 482: 90-96.
- [5] SANTE R D. Fibre optic sensors for structural health monitoring of aircraft composite structures: recent advances and applications[J]. Sensors, 2015, 15(8):

- 18666-18713.
- [6] LI Y H, GUAN K S, HU Z H. Fiber optic displacement measurement model based on finite reflective surface[J]. *Optics & laser technology*, 2016, 84: 32-39.
- [7] NISHIO M, MIZUTANI T, TAKEDA N. Structural shape reconstruction with consideration of the reliability of distributed strain data from a Brillouin-scattering-based optical fiber sensor[J]. *Smart materials and structures*, 2010, 19(3): 035011.
- [8] NISHIYAMA M, SASAKI H, WATANABE K. A deformation sensitive pad-structure embedded with hetero-core optic fiber sensors[J]. *Sensors and actuators A: physical*, 2006, 136(1): 205-211.
- [9] KANG J. Research on deformation, impact and vibration of flexible structure based on distributed optical fiber[D]. Nanjing: Nanjing University of Aeronautics and Astronautics, 2018. (in Chinese)
- [10] QIAO X P, ZHU X J, ZHANG H S, et al. Surface reconstruction algorithm based on surface splicing[J]. *Journal of vibration, measurement & diagnosis*, 2013, 33(S1): 160-163. (in Chinese)
- [11] SAKIYAMA F I H, LEHMANN F A, GARRECHT H. Structural health monitoring of concrete structures using fibre-optic-based sensors: a review[J]. *Magazine of concrete research*, 2019, 73(4): 174-194.
- [12] JURASZEK J. Application of fiber optic FBG techniques in analysis of strain in engineering machines[J]. *New trends in production engineering*, 2019, 2(1): 480-485.
- [13] GAO L, ZHANG Q H, LI E B, et al. Strain monitoring of combustible gas implosion test based on fiber Bragg grating[J]. *Shock and vibration*, 2019, 2019: 1-17.
- [14] LI D T. Flexible structure deformation monitoring technology research based on distributed optical fiber[D]. Nanjing: Nanjing University of Aeronautics and Astronautics, 2017. (in Chinese)
- [15] WANG C. 3D shape detection method of soft manipulator based on fiber Bragg grating sensor[J]. *Chemical automation and instrument*, 2015, 42(10): 1130-1133. (in Chinese)
- [16] HE K, ZENG J, LIN Q H, et al. Research on spatial deployable structure deformation and vibration monitoring with distributed optical fiber[J]. *Chinese journal of scientific instrument*, 2018, 39(2): 56-65. (in Chinese)